Radar Remote Sensing of Wind-Driven Land Degradation Processes in Northeastern Patagonia

H. F. del Valle* and P. D. Blanco Centro Nacional Patagónico (CENPAT)
G. I. Metternicht United Nations Environment Programme (UNEP)
J. A. Zinck International Institute for Geo-Information Science and Earth Observation (ITC)

Wind-driven land degradation negatively impacts on rangeland production and infrastructure in the Valdes Peninsula, northeastern Patagonia. The Valdes Peninsula has the most noticeable dunefields of the Patagonian drylands. Wind erosion has been assessed at different scales in this region, but often with limited data. In general, terrain features caused by wind activity are better discriminated by active microwaves than by sensors operating in the visible and infrared regions of the electromagnetic spectrum. This paper aims to analyze wind-driven land degradation processes that control the radar backscatter observed in different sources of radar imagery. We used subsets derived from SIR-C, ERS-1 and 2, ENVISAT ASAR, RADARSAT-1, and ALOS PALSAR data. The visibility of aeolian features on radar images is mostly a function of wavelength, polarization, and incidence angle. Stabilized sand deposits are clearly observed in radar images, with defined edges but also signals of ongoing wind erosion. One of the most conspicuous features corresponds to old track sand dunes, a mixture of active and inactive barchanoid ridges and parabolic dunes. This is a clear example of deactivation of migrating dunes under the influence of vegetation. The L-band data reveal details of these sand ridges, whereas the C-band data only allow detecting a few of the larger tracks. The results of this study enable us to make recommendations about the utility of some radar sensor configurations for wind-driven land degradation reconnaissance in mid-latitude regions.

Published in J. Environ. Qual. 39:62–75 (2010).
doi:10.2134/jeq2009.0071
Published online 20 Nov. 2009.
Received 27 Feb. 2009.
*Corresponding author (delvalle@cenpat.edu.ar).

677 S. Segoe Rd., Madison, WI 53711 USA

Wind Erosion in the Valdes Peninsula

Land degradation by wind erosion affects large areas of the world's arid and semiarid lands (Lal, 2001). Redistribution of material by wind occurs at multiple spatial and temporal scales (Gibbens et al., 1983; Chadwick et al., 1999; Okin et al., 2001; Prospero et al., 2002). In the Valdes Peninsula, northeastern Patagonia (Argentina), wind erosion negatively impacts on rangeland production, farm infrastructure, and ecosystem health (Rostagno 1981; Gagliardini et al., 1994; Súnico 1996; Blanco et al., 2008). In these flat open fields, wind erosion is a major problem affecting also the quality of both air and water points (del Valle et al., 2000).

The Valdes Peninsula has the most noticeable dunefields of the Patagonian drylands, covering an area of approximately 884 km^2 (del Valle et al., 2008). The use of remote sensing provides a synoptic view at regional level that allows identifying sand mobilization along discrete transport paths. Sand is blown from the western coast of the peninsula to the Atlantic Ocean in the east (del Valle et al., 2008).

There is evidence that dune activity has been more extensive and intense in the past throughout the Valdes aeolian geomorphic system. Earlier dune systems, climbing and falling dunes (sand ramps), discontinuous sand mantles in gravel plains, and sandy beach ridges are now vegetation-covered (Bouza et al., 2002, 2005). Sand sheets and dunes of different types are stabilized by psammophytic species such as *Sporobolus rigens* and *Hyalis argentea* (Bertiller et al., 1981). These relict aeolian landforms would have been formed in a periglacial environment (Iriondo and García, 1993; Trombotto 1998). Dunes currently active seem to have developed from a series of dune megapatches (colony of dunes) of different sizes, each of which represents an episode of sediment input or reworking of existing sand dunes (del Valle et al., 2008).

Wind erosion in the Valdes Peninsula produces strong signals of environmental changes leading to desertification in the form of deflating surfaces, dust storms, and migrating sand dunes (del Valle et al., 2008). Two critical factors that influence the severity

H.F. del Valle and P.D. Blanco, Centro Nacional Patagónico (CENPAT), Consejo Nacional de Investigaciones Científicas y Técnicas (CONICET), Área Científica Ecología Terrestre; Boulevard Almirante Brown 2915, (U9120ACF) Puerto Madryn (Chubut), Argentina. G.I. Metternicht, United Nations Environment Programme (UNEP), Regional Office for Latin America and the Caribbean, Clayton, City of Knowledge- Avenida Morse, Edificio 103, Panamá city, Panamá. J.A. Zinck, International Institute for Geo-Information Science and Earth Observation (ITC), Enschede, Netherlands.

Abbreviations: EEI, edge enhancing index; SAR, synthetic aperture radar; SSI, speckle suppression index.

of wind erosion are the percent of vegetation cover and the type of terrain surface (Bertiller et al., 1981; Rostagno, 1981; Bouza et al., 2005). Short-term variation in wind erosion is controlled by factors such as high interannual rainfall variability, droughts, localized wildfires, and livestock grazing (Blanco et al., 2008).

Remote Sensing of Wind-Induced Processes

Earlier attempts to identify wind erosion features mostly used the visible and infrared wave bands (Carter and Houghton, 1981; Paisley et al., 1991; Chen et al., 1998; Zobeck et al., 2000; Okin and Gillette, 2001; Collado et al., 2002). Data provided by the Advanced Spaceborne Thermal Emission and Reflection Radiometer (ASTER) have a significant advantage over previous datasets because of the combination of high spatial resolution (15–90 m) and enhanced multispectral capabilities, particularly in the thermal infrared (TIR) atmospheric window (8–12 μm) of the Earth where common silicate minerals are more easily identified (Ramsey et al., 1999; Ogawa et al., 2002). However, the origins of the signatures detected by imaging radars are fundamentally different than those detected by visible and infrared systems. Data collected using synthetic aperture radar (SAR) have the potential to provide information on the geometry of sand dunes and other aeolian features because of the sensor's susceptibility to changes in the structure of surface features. This is particularly important in areas where dunes are not pronounced and, therefore, optical remote sensors may fail to reveal the geometry of the dunes. Previous research has shown that SAR imagery can also provide useful information for distinguishing stable vegetated areas from bare areas of active sand dunes (Blom and Elachi 1981; Lancaster et al., 1992; Greeley and Blumberg 1995; Blumberg, 1998; Blanco et al., 2009).

There are significant differences between active microwave and optical wavelengths in the mechanics of imaging and in the measured characteristics of a target (Kasischke et al., 1997). Because of the side-looking illumination geometry, radar images are distorted to some extent. In addition, the radar waves are most sensitive to surface roughness at scales near the radar wavelength (Dobson et al., 1997).

Radar signals depend also on the target's dielectric constant that is a measure of how well electromagnetic waves couple with a given type of material (rock, regolith, soil). The low soil moisture in desert areas increases the importance of soil roughness, vegetation, and soil volume scattering in the radar backscatter. Therefore, the geometric and electromagnetic interactions of radar waves with natural surfaces must be considered for accurate interpretation of SAR images (Fung, 1994; Greeley et al., 1997).

In semiarid and arid landscapes, the vegetation cover is sparse and the terrain surfaces are usually not fully stabilized. For radar data, this has the consequence that the scattering is originated mainly by the surface roughness that is in turn a dynamic geomorphic property. A returned radar signal varies considerably in response to variations in terrain morphology, topography, and surface cover (Ridley et al., 1996; Blumberg, 1998; Levin et al., 2008). To explain these variations, it is necessary to understand the nature of the interaction between active microwave radiation and surface properties, and determine what soil surface features are suitable for use as spectral indicators.

In the dunefields of the Valdes Peninsula, vegetation cover, species composition, aeolian landform types, and soil surface conditions form a variable continuum influenced by climate and grazing that lacks discrete land use patterns (Blanco et al., 2008; del Valle et al., 2008). In such conditions, active microwave remote sensing tends to be highly site-specific, and that allows maximizing the extraction of statistically distinct backscatter patterns of the dunefields.

Since radar backscatter is highly dependent on the geometric and electric properties of a given terrain, studying the angular and polarimetric behaviors of this backscatter is the key to extracting structural information about the terrain (Dobson et al., 1995). Usually in active microwave remote sensing applications, the SAR parameters are known, but the relationship between target and measured signals has to be investigated.

Objectives of the Study

The objectives of this study were to assess the potential of different SAR imageries for detecting and interpreting structural attributes of the terrain surface and the vegetation cover that can be used for mapping, and develop interpretative keys that link the SAR-based structural attributes to wind-driven land degradation processes.

We attempt to show the dependence of the radar backscatter on four primary factors related to wind erosion, namely surface roughness, soil moisture, local incidence angle, and vegetation cover.

This study is part of a multi-scale research on deserts and semideserts using spacecraft-borne sensors (SIR-C/XSAR, ERS/SAR, ENVISAT ASAR, RADARSAT, ALOS/PALSAR, TERRASAR-X, COSMO-SkyMed, and the forthcoming TERRASAR-L and SAOCOM) and aircraft-borne sensors (SARAT: synthetic aperture radar airborne transport, Argentinean project). The approach of nested scales is most appropriate for implementing successful strategies against wind erosion in carefully chosen areas.

Materials and Methods

Study Site and Environmental Characteristics

The Valdes Peninsula lies on the east coast of the Argentinean Patagonia (42° 05′–42° 53′ S and 63° 30′–64° 37′ W). It is surrounded by the San Matías Gulf to the north, the San José Gulf to the northwest, the Nuevo Gulf to the southwest, and the Atlantic Ocean to the east and south. Observations on wind-driven degradation processes were performed in an area of 1231 km^2 centered at 42° 43′ S, 63° 57′ W (Fig. 1).

The southern sector of the peninsula is affected by the progression of several fronts of active sand dunes grouped in discrete megapatches. Dune mobility is high because of prevailing strong winds that cause eastward sand migration at an average speed of 9.1 ± 2.7 m yr^{-1} (del Valle et al., 2008). Air circulation is strongly influenced by the shape of the coastline, while the dunefields are very much related to the loose sediments of this windward coast that is unique in northeastern Patagonia.

The climate is temperate arid, with annual temperature and rainfall averages of 13°C and 231 mm, respectively, for the period 1912 to 2008. The proximity to the sea influences the peninsular climate

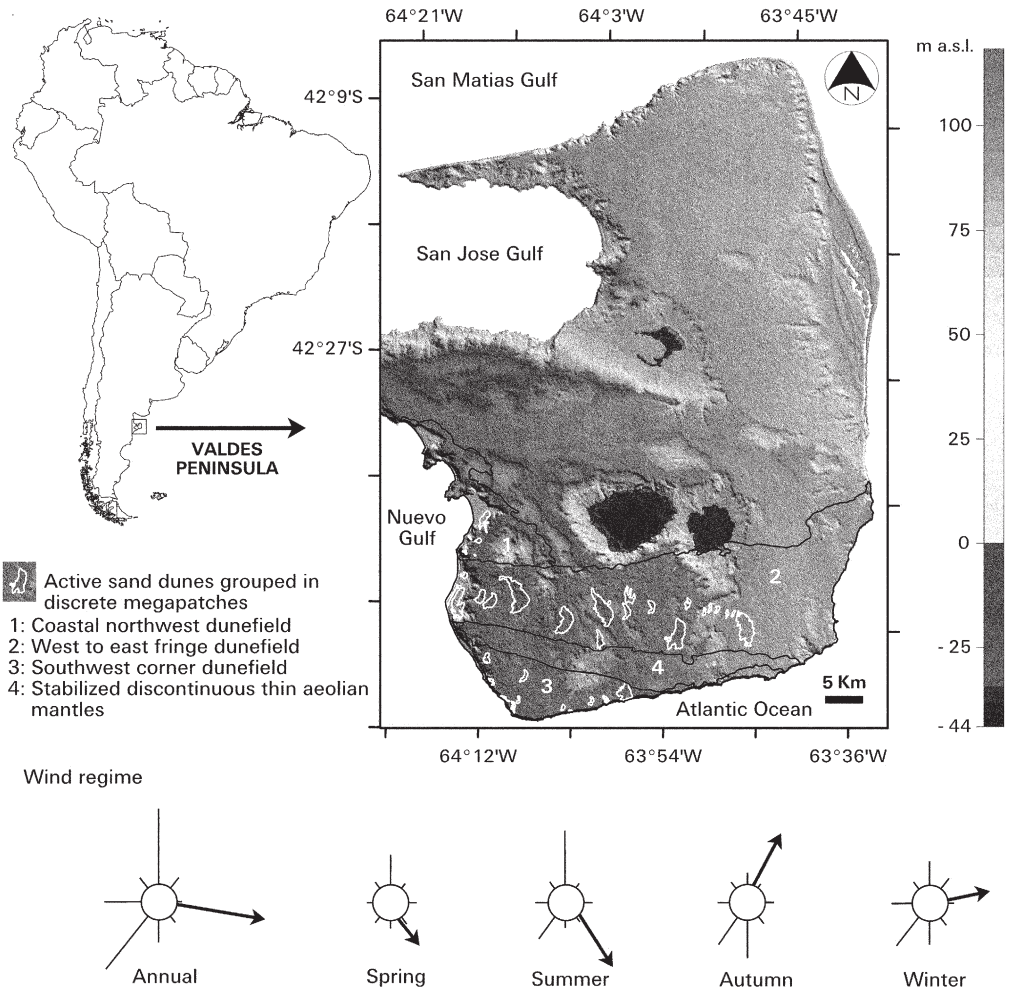

Fig. 1. Map of the study area showing the aeolian system of the Valdes Peninsula, northeastern Patagonia (Argentina). This figure was extracted from the SRTM 90m DEM´s (http://srtm.csi.cgiar.org/). The white polygons represent discrete active sand dune megapatches, digitized on a Landsat ETM+ image (del Valle et al., 2008). The regional annual wind rose shows vectors of wind intensity in northeastern Patagonia. The north wind intensity increases eastwards at the latitude of the Valdes Peninsula. The west component overwhelmingly prevails throughout the area. Seasonal wind regimes refer to spring (September–November), summer (December–February), autumn (March–May), and winter (June–August).

much more than that of the adjacent mainland, especially in reducing the annual temperature amplitude (10.6°C in the peninsula vs. 14.0°C inland), the number of days of frost (< 20 vs. 40), and the interannual rainfall fluctuations (coefficient of variation of 30% vs. 44%) (Barros and Rivero, 1982). There is no clearly defined rain season in the area. However, rainfall is more frequent in autumn and winter, thus aridity is somewhat mitigated during this period of the year. The Valdes Peninsula shares with the rest of Patagonia the same windy conditions, with an annual mean wind speed > 4.0 m s^{-1}. However, westerly winds are less predominant here, while north and northeast winds become more frequent because of the easternmost position of the peninsula and the stronger influence of the southwest Atlantic anticyclone (Paruelo et al., 1998).

Gravel deposits of Pliocene-Pleistocene age, locally named "Rodados Patagónicos", cover parts of the Valdes Peninsula. Tertiary (Miocene) marine sediments are exposed on the seashore cliffs and in the erosion fronts of tectonic depressions. Our study area includes gravel plains and sand deposits (Haller et al., 2000).

The vegetation is transitional between the southern portion of the phytogeographic province called Monte (desert shrub) and the northern portion of the Patagonian province (León et al., 1998). The following communities are widespread throughout the study area: (i) grass steppe of *Sporobolus rigens* and *Stipa tenuis*, (ii) mosaic of grass steppe of *S. rigens* and *S. tenuis* and scrub steppe of *Hyalis argentea*, (iii) grass steppe of *Piptochaetium napostaense*, *S. tenuis* and *Plantago patagonica*, and (iv) mosaic of grass steppe of *P. napostaense*, *S. tenuis*, and *P. patagonica* and shrub-grass steppe of *Chuquiraga avellanedae* and *S. tenuis* (Bertiller et al., 1981). On vegetated dunes, the cover is up to 60 to 80%.

Sheep (*Ovis aries*) raising, mainly for wool production, is the main land use type of the Valdes Peninsula rangelands. Sheep were introduced at the beginning of the last century (Defossé et al., 1992) and are now raised in large farms (5000–10,000 ha) consisting of several paddocks around shared water points. Grazing disrupts the vegetation cover of the dunes (Blanco et al., 2008) and promotes wind deflation, as shown by increasing appearance of blowouts.

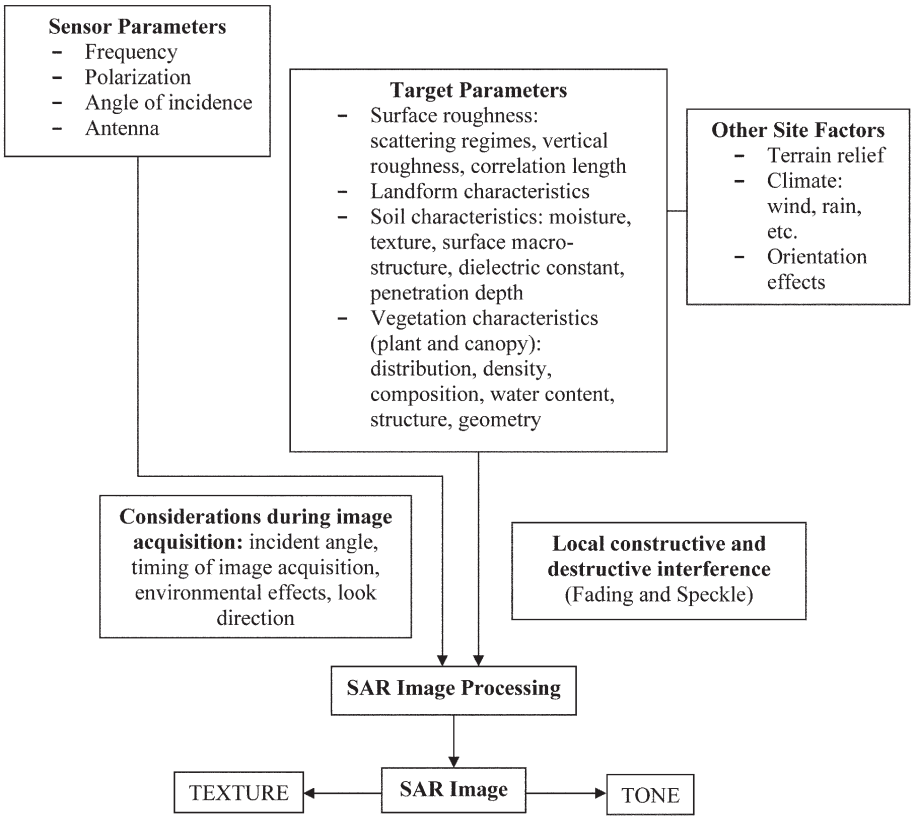

Fig. 2. Synthetic aperture radar (SAR) instrument configuration and environmental conditions determining the signal-object in a radar image.

Database and Digital Image Processing

Parameters that Influence the Radar Signal

The SAR image formation depends on the combination of the sensor parameters with those of the target, the atmospheric conditions at the moment of the data acquisition, as well as the mechanisms of interaction and the processing level realized previous to the distribution of the data (Fig. 2). The response of the radar shows the interaction signal-object (forms of dispersion of the signal) that determines the gray value of the image and its interpretation.

Synthetic Aperture Radar Data

Ten SAR images were acquired over the study area by the SIR-C, ERS-1 and 2, ENVISAT ASAR, and RADARSAT-1, as well as the ALOS PALSAR. The SAR data were converted to polarimetric imagery and the components of the microwave backscatter returning to the SAR antenna were stored in a compressed Stokes matrix format (van Zyl and Ulaby, 1990). Details of the SAR data configurations and published calibration values are shown in Table 1. No significant rainfall event was recorded in the month previous to the SAR image acquisition, and relative air humidity was typically low at that time. Aspect and prevailing wind data were recorded in the study area.

Synthetic Aperture Radar Image Preprocessing

Satellite data were georeferenced and co-registered to analyze the synergistic effect of various polarizations and incidence angles. For proper integration of various layers generated from different-resolution satellite datasets, feature-to-feature matching was considered more important. Permanent features like road crossings were few and also not so prominent because of their narrow dimensions, and were difficult to observe in the images. Features like drainage bends, sharp ridge curves, isolated features and some permanent structures were considered for ground control points (GCPs). To ensure accurate data overlay at pixel level, 50 metallic roofs of farmland buildings were used as reference points for geometric adjustment. They appear as very bright objects in the SAR images due to the high returns caused by the corner reflector effect, and can be identified by their rectangular or square shapes (del Valle et al., 2009). Additionally, a few geometric differences and distortions in data processing (because of relief displacement attributed to the geometry of the ERS 1 satellite image) were recognized and estimated with ground truth (GPS geodesic) and using the SRTM elevation data (http://srtm.csi.cgiar.org/).

The images were rectified and transformed to a Transverse Mercator cartographic projection, applying a cubic convolution interpolation technique, while retaining pixel spacing at 12.5 m (SIR-C, ERS-1 and 2, ENVISAT ASAR) and 6.25 m (RADARSAT-1, ALOS PALSAR). The root-mean-square (RMS) transformation errors were about 3.7 m for RADARSAT-1 and ALOS PALSAR, and 9.5 m for SIR-C, ERS-1 and 2 and ENVISAT ASAR.

The backscattering coefficients (σ^0) of selected areas were calculated by creating a model in the Erdas Imagine 9.2 software (ERDAS Inc., 2008). The basic equations used for the calculation of σ^0 are as follows:
SIR-C (Freeman, 1995):

Table 1. Characteristics of Earth orbital synthetic aperture radar (SAR) systems.

Characteristics	SIR-C SAR†	ERS 1–2 SAR‡	ENVISAT§	RADARSAT-1¶	ALOS/PALSAR #
Acquisition Date (dd-mm-yy)	05–10–94	09–07–92 22–02–98 28–07–01 02–05–02	11–04–04 14–07–06	01–01–05	14–02–07 17–02–08
Product type	Multi-Look Complex (MLC)	Precision Image (PRI)	ASAR Alternating Polarization Mode Precision Image (ASA_APP_1P)	SAR Georeferenced Fine Resolution (SGF)	Level 1 Multi-look Data (H1.5_UA)
Orbit direction	Ascending (east looking)	Descending (west looking)	Descending (west looking)	Descending (west looking)	Ascending (east looking)
SAR Band	C, L	C	C	C	L
Wavelength, cm	5.8, 23.9	5.6	5.8	5.7	24
Polarization	HH, HV	VV	VV, HH VV,VH	HH	HH
Incidence angle, degree	55.8	23	23	35	34.3
Frequency, GHz	5.3, 1.25	5.25	5.25	5.3	1.27
Pulse bandwidth, MHz	10–20	15.5	9	11.6–17.3	28–14
Number of looks	4	1, 2	1	1	2
Nominal ground range resolution, m	25	25	30	9	10
Nominal Azimuth Resolution, m	30	30	30	8	10
Line/pixel spacing, m	12.5	12.5	12.5	6.25	6.25
Noise equivalent σ_0, dB	–34 (C-band) –50 (L-band)	–24.8	–20.4	–20	–31.1
Wind direction, Wind speed, m s^{-1}	SW, 1.8	SE, 3.1 NE, 5.8 SW, 2.1 W, 8.1	NE, 2.1 W, 0.5	SW, 7.0	NE, 1.3 SW, 2.9

† Freeman (1995).

‡ Laur et al. (2004).

§ Desnos et al. (2000).

¶ CSA (2000).

JAXA (2008).

C band HH dB = (DN/(255/25)) - 25

C band HV dB = (DN/(255/25)) - 35

L band HH dB = (DN/(255/35)) - 35

L band HV dB = (DN/(255/35)) - 45

ERS-1&2 (Laur et al., 2004):

$$\sigma^0_{i,j} = \frac{CN^2_{I,J}}{K_{SAR\ ERS}} \times \frac{\sin_{(\alpha_{i,j})}}{\sin_{(\alpha_{ref})}} \quad \begin{matrix} i=1\_L \\ j=1\_M \end{matrix}$$

where:

$\sigma^0_{i,j}$: Backscattering coefficient of pixel (i, j)

$K_{SAR\ ERS}$: Absolute constant of calibration

$CN^2_{I,J}$: intensity value of pixel (i, j)

α_{ref}: reference incidence angle (23°)

$\alpha_{i,j}$: incidence angle on pixel (i, j)

ENVISAT-ASAR (Desnos et al., 2000):

$$\sigma^0_{i,j} = \frac{CN^2_{I,J}}{K_{ASAR\ Envisat}} \sin_{(\alpha_{i,j})} \quad \begin{matrix} i=1\_L \\ j=1\_M \end{matrix}$$

where:

$\sigma^0_{i,j}$: Backscattering coefficient of pixel (i, j)

$K_{ASAR\ Envisat}$: Absolute constant of calibration

$CN^2_{I,J}$: intensity value of pixel (i, j)

$\alpha_{i,j}$: incidence angle on pixel (i, j)

RADARSAT-1 (CSA, 2000):

The relationship between radar brightness (β^0) and radar backscatter coefficient (σ^0) is:

$$\sigma^0_j = \beta^0_j + 10 \times \log_{10}(\sin I_j)\,\mathrm{dB}$$

where: I_j is the incidence angle at the j range pixel. This formula assumes that the earth is a smooth ellipsoid at sea level.

ALOS PALSAR (JAXA, 2008):

$$\sigma^0_i(dB) = 20 \log_{10} DN_i + \mathrm{Kdb}$$

where:

DN: digital number

Kdb: Absolute constant of calibration

For speckle suppression, three polarimetric filters with a 3 by 3 pixels window size and one iteration were used, namely Gamma Map (SIR-C, ERS-1 and 2, RADARSAT-1), Mean also known as "boxcar" (ENVISAT-ASAR), and Lee (ALOS PALSAR). The performance of each polarimetric filter was assessed based on the criteria of Sheng and Xia (1996), that is, the speckle suppression index (SSI) and the edge enhancing index (EEI). The best filter should be able of retaining linear land cover features (highest EEI obtained) and homogenizing polygonal land cover features (lowest SSI obtained).

Table 2. Landforms, cover type, major species, roughness, and their tone on radar image.

Class	Landforms	Land cover structure class	Most common species	Radar signatures†	
				C-band	L-band
1	Foreshore sand beaches	Unvegetated desert sand beaches		Dark	Dark
2	Cliffs scarp (wind abrasion), upper beaches and sand ramps	Generally unvegetated		Bright and Dark	Bright and Dark
3	Coastal and inland sand dunes	Unvegetated sand dunes		Dark, Bright	Dark, Intermediate
4	Interdune	*Erg* generally without vegetation cover		Intermediate	Intermediate
5	Scald-scabby	Flat surface created by aeolian deflation of the sand mantle; surface characterized by small pebble deposits and sparse vegetation	*Stipa tenuis*	Bright, Intermediate	Bright, Intermediate
6	Stabilized dunefields with conspicuous dune crest	Grass steppe. Mixed short grasses (10–30 cm) with some shrubs (10 cm). 70–80% vegetation cover	*Sporobolus rigens, Stipa tenuis*	Intermediate, Dark	Intermediate, Bright
7	Stabilized dunefields with conspicuous dune crest	Shrub steppe with grasses. Closed shrub (50 cm) with very short grasses (5 cm). 70% vegetation cover	*Hyalis argentea, Stipa tenuis*	Intermediate, Dark	Intermediate, Bright
8	Stabilized dunefields with conspicuous dune crest and aeolian deflation areas	Mosaic of grass steppe with some shrubs. Mixed grasses (10–30 cm) and shrubs (50 cm). 70–80% vegetation cover	*Sporobolus rigens, Stipa tenuis, Hyalis argentea*	Intermediate, Dark	Intermediate, Bright
9	Stabilized dunefields with conspicuous dune crest and aeolian deflation areas	Grass steppe with some shrubs. Mixed short grasses (20 cm) and shrubs (50–150 cm). 60–70% vegetation cover	*Piptochaetium napostaense, Stipa tenuis, Plantago patagonica*	Intermediate, Dark	Intermediate, Bright
10	Stabilized discontinuous thin aeolian mantles in gravel plains	Mosaic of grass steppe and shrub-grass steppe. Mixed short grasses (20 cm) and shrubs (50–200 cm). 60–70% vegetation cover	*Piptochaetium napostaense, Stipa tenuis, Plantago patagonica, Chuquiraga avellanedae*	Intermediate, Bright	Intermediate
11	Coastal dunes with wind abrasion	Shrub steppe. Mixed shrubs (70–110 cm). 50% vegetation cover	*Senecio filaginoides, Mulinum spinosum*	Intermediate, Dark	Intermediate, Dark
12	Stabilized discontinuous thin aeolian mantles in gravel plains	Shrub-grass steppe. Shrubs (80–100 cm) with grasses (10–20 cm). 40–60% vegetation cover	*Chuquiraga avellanedae, Stipa tenuis*	Intermediate, Bright	Intermediate
13	Temporary and permanent saltlakes	Generally unvegetated		Very dark	Very dark

† Surface roughness types (Image tone): Smooth (Dark), Intermediate (Intermediate), and Rough (Bright).

Analysis of the Synthetic Aperture Radar Backscatter

Variables related to the radar design and environmental settings were analyzed to better understand the behavior of the radar-backscattering signal. In our environmental conditions, four factors control the variations of the backscattering coefficient, namely surface roughness (influenced by terrain features, vegetation physiognomy, and wind conditions at the time of the radar overpass), soil moisture, local incidence angle, and vegetation cover. The backscattering intensity changes with these parameters and produces image brightness variations, expressed as changes in the pixel gray levels of the images.

The qualitative interpretation applied in this research did not require detailed roughness measurements but knowledge about the environmental variables that most likely influence changes in image brightness. Table 2 describes the major species, landforms, and vegetation cover types of the dunefields, with their surface roughness and tone on each radar band image. Some examples of land cover class are showed in Fig. 3a-f.

The relationships between backscatter (σ^0) and biophysical properties were analyzed for the following land cover classes: (i) scald-scabby areas (deflation areas), (ii) cliff scarps (wind abrasion), (iii) discontinuous thin aeolian mantles in gravel plains, (iv) interdunes, (v) closed scrubs, (vi) mosaic grass-scrub steppe with deflation areas, (vii) grass-scrub steppe without deflation areas, (viii) old track sand dune, and (ix) active sand dune megapatches. We used ANOVA and Tukey's multiple comparison tests to evaluate the significance of differences between means backscatter of the land cover classes. The distribution of data for all variables was found to be normal, so the data were not normalized or otherwise transformed.

Ground truth was gathered in 1978 (Rostagno, 1981; Bertiller et al., 1981), 1994 to 1996 (Gagliardini et al., 1994; del Valle et al., 2000), and 2001 to 2008 (Bouza et al., 2002, 2005; del Valle et al., 2008; Blanco et al., 2008, 2009). Ninety training sites (10 polygons of 100–140 pixels per class) were located using a GPS with 4-m accuracy. Several sampled sites were revisited and photographed to document wind erosion and other aeolian features. Table 3 summarizes these studies in relation with the nature of the land degradation. Each sampled site was described in terms of land use, geomorphology, vegetation, and soil morphology (USDA, 2003). Past wind erosion was identified using visual field indicators such as bare soil surfaces, deflation hollows, desert pavements, wind scours between plants, drifted or rippled terrain surfaces, pedestal plants, exposed roots, sand deposition on the leeward side of plants and obstacles, subsoil exposure, and reduced plant growth.

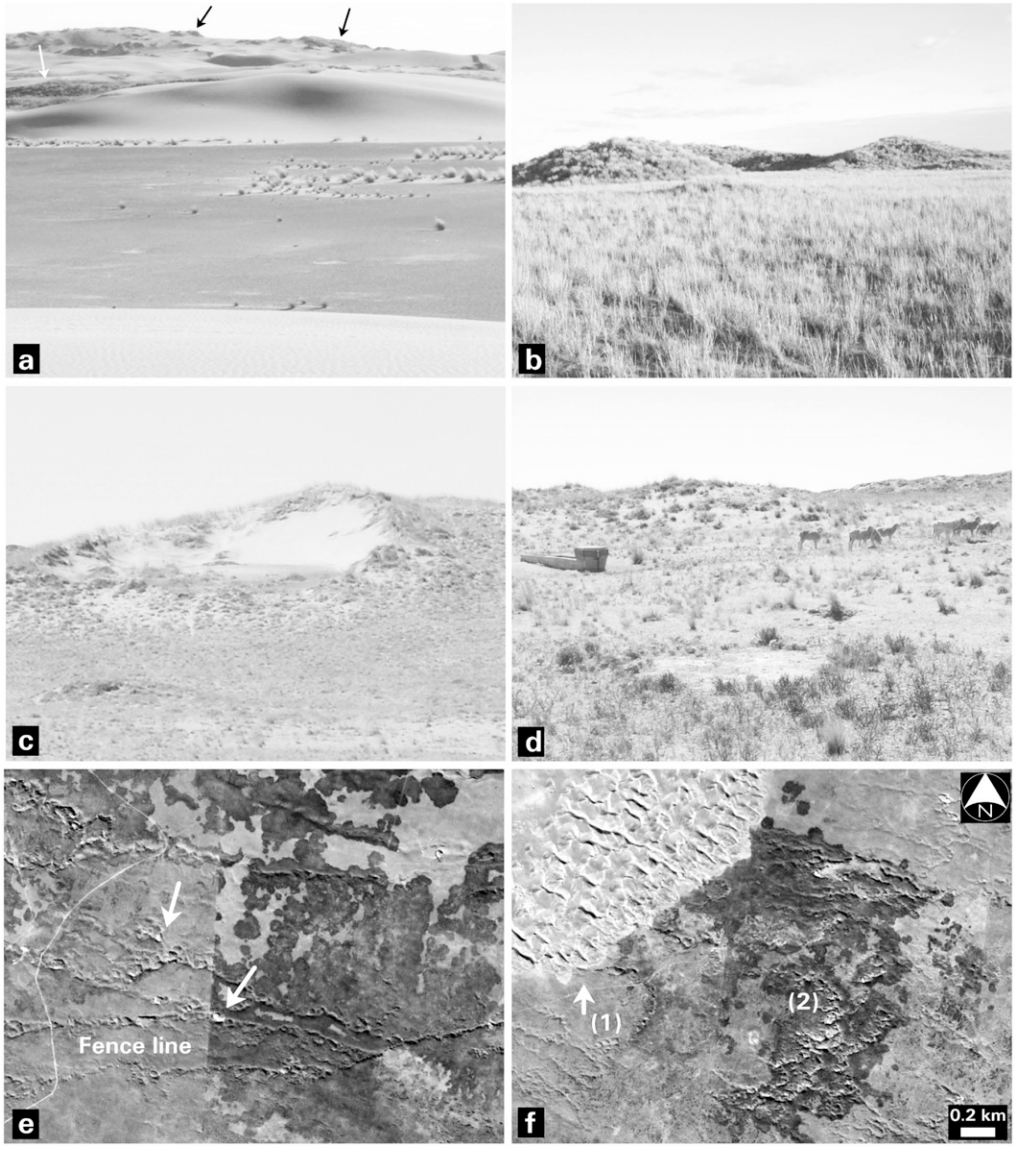

Figure 3a-f. 3a. Inland colonies of sand dunes showing the interdune space with sparse vegetation and desert pavement. The arrows point to psammophytic species (mainly the native *Hyalis argentea*) that try to recolonize the dune. 3b. Stabilized dunes with conspicuous dune crests. Mosaic of grass steppe with some shrubs. 3c. Grazing impact on a vegetated dunefield showing a deflation hollow (blowout). 3d. Site showing high density of blowouts in the proximity of a water point. 3e. Subset of an ALOS PRISM image (24 Mar. 2007), with 2.5 m spatial resolution, showing contrast in land management (fence line). Right: closed shrub cover of *Hyalis argentea*. Left: mixed short grasses of *Sporobolus rigens* with some shrubs. The arrows point to inactive parabolic dunes resulting from the deactivation of migrating dunes under the influence of vegetation. 3f. Subset of an ALOS PRISM image (24 Mar. 2007) showing (1) an active sand dune megapatch, and (2) inactive parabolic dunes with some blowouts.

Results and Discussion

Multisensor Image Interpretation

The ANOVA results are presented in Table 4. Land cover classes predicted the differences in backscatter values (σ^0) for all the radar images. Different letters indicate significant differences ($p < 0.05$) among classes. The mean and standard deviation backscatter (σ^0) estimates for each land cover classes were spatially and temporally highly variable. While the classes exhibited the same general trend that we observed on the landscape scale, namely a low backscatter (σ^0) with the aeolian features more conspicuous of the class and the wind condition.

L-band from SIR-C and ALOS PALSAR separate the classes more than C band does. This may be due to the fact that L-band penetrates deeper in the soil and has better sensitivity of SAR to surface roughness (Greeley and Blumberg, 1995; Blumberg et al., 2004). The L-HH has greater penetration to underlying soil and L-HV is more sensitive to the target volume. The radar wavelengths and polarizations that improve the contrast among the dunefields and the surrounding sand mantle of the gravel plain are (in descending order): L-HV (SIR-C), L-HH (SIR-C and ALOS PALSAR) and C-HH (RADARSAT-1). This will be discussed in detail further in the article.

Smaller look angles (≤ 35°) tend to enhance the internal structure of sand dune megapatches, while larger look angle

Table 3. Summary of documented local studies named in the text.

References	Spatial scale†	Temporal scale‡	Data characteristics	Basis of erosion component	Nature of the land degradation	Land cover classes recognized (total sites visited)§
Rostagno (1981)	L	A	Climate, soil types	Physically based	Soil erosion	GP, CS, M1, D (15)
Bertiller et al. (1981)	L	A	Vegetation types	Physically based	Vegetation degradation	GP, CS, M1, M2, D (15)
Gagliardini et al. (1994)	F+L	A	Landforms, surface roughness	Process-based	Deflation, accumulation	AD, C, GP, I, OT, D (20)
del Valle et al. (2000)	F+L	M	Landforms, surface roughness, soil surface, wind, vegetation cover	Source-based, physical condition based	Deflation, accumulation, path sand transport	AD, GP, CS, M1, OT, D (33)
Bouza et al. (2002)	P+F	A	Soil types	Physically based	Soil erosion, soil buried	GP, M1 (10)
Bouza et al. (2005)	P	A	Soil types	Physically based	Soil erosion, soil buried	GP, M1 (10)
del Valle et al. (2008)	F+L	M	Wind, landforms, surface roughness, vegetation cover	Climate records, index, source-based, physical condition based	Deflation, accumulation, path sand transport	AD, C, CS, M1, OT, D (33)
Blanco et al. (2008)	P+F+L	A	Climate, landforms, surface roughness, wind, vegetation cover	Process-based	Deflation	OT, D (20)
Blanco et al. (2009)	P+F+L	A	Landforms, surface roughness, wind, vegetation cover	Process-based	Deflation, accumulation	OT, D (20)
This paper	F+L	M	Surface roughness, wind, vegetation cover	Physical condition based	Deflation, accumulation, dust flux, landscape erodibility, hazard	AD, C, GP, I, CS, M1, M2, OT, D (90)

† P: plot, F: field, L: local.

‡ A: annual, M: multi-temporal.

§ AD: scald-scabby areas (deflation areas), C: cliff scarps (wind abrasion), GP: discontinuous thin aeolian mantles in gravel plains, I: interdunes, CS: closed scrubs, M1: mosaic grass-scrub steppe with deflation areas, M2: grass-scrub steppe without deflation areas, OT: old track sand dune, and D: active sand dune megapatches.

(55.8°, like SIR-C) reflect the surface roughness and texture (Greeley and Blumberg, 1995). The HH and VV backscatters, particularly at small incident angles (like ERS and ENVISAT ASAR), are significantly increased when the radar looks perpendicular to the direction of the dune face. The topography and orientation of the sand dunes produce high backscatter in a descending orbit (west looking).

Wind influences the surface roughness (ERS 1 & 2, see Table 1), especially for vegetated and nonvegetated surfaces where the wave action increases the backscatter (high values). The subtle roughness difference between the two bands L-HH, with exact difference of a year (ALOS PALSAR), it could also be due to the influence of the wind.

Active Multiwavelength Analysis: The SIR-C Data

On Fig. 4a-c, the stabilized dunefields with conspicuous crests can be clearly identified by their intermediate gray tones (medium backscatter). Active sand dunes show smooth dry dark surfaces (low backscatter). Temporary or permanent salt lakes and sand beaches correspond to very dark surfaces (specular scattering, low backscatter). The bright linear reflections represent steep crests of inactive sand ridges. The sparse vegetation and pebbles that cover the gravel plains ("Rodados Patagónicos") produce moderate radar returns and appear as light gray tones, in contrast to sand covered areas. Often, lighter and darker tones are paired in parallel lines because of alternatively illuminated and shadowed shrubs or clumps of shrubs (mostly shrubs of *Chuquiraga avellanedae*) above the overall ground cover (del Valle and Blanco, 2006). Narrow sand beaches, gullies, and cliff scarps appear in bright white tones (rough surface, high backscatter).

In general, tone variations of the SAR images are more relevant to spectral or dynamic properties than to surface roughness (Qong, 2000). However, windblown sand easily produces changes in surface roughness and could be the cause of the temporal variations of the backscatter coefficient (Prigent et al., 2005). Sand movement randomly changes the micro-geometry of the sand scatters on the terrain surface. The very dark features of mobile sand over a bright matrix are not only direct evidence of sand mobility, but they also effectively delineate the outlines of active dunes and visually indiscernible thin sand sheets (Liu et al., 1997; Stephen and Long, 2004).

Spatial patterns of tone and texture variations are much better recognized on the L-band (Fig. 4b and Fig. 4c) than on the C-band images (Fig. 4a). The L-band images show various shades of gray that indicate different levels of low vegetation density and eroded soils, and reflect degrees of vulnerability to wind erosion (del Valle and Blanco, 2006). There are subtle differences between the L-HH and L-HV bands to detect and interpret wind erosion features. At steep incident angles such as in the case of SIR-C (55.8°), HH images tend to provide more information about the soil condition, while the C-HV band provides complementary information to the former.

Multitemporal Analysis: The ERS Data

Wind causes local "noise" effect on the temporal backscatter signal (Fig. 5a-d). Thus, the radar imagery can contribute to overcome the lack of local wind data, as is the case in our study area (del Valle et al., 2008). Figure 5c and Fig. 5d show strong western winds, resulting in enhanced radar backscattering (subsets of ERS-2 images, C-band VV). The images reveal

Table 4. Mean and standard deviation backscatter (σ^0) per image for land cover classes.

RADAR	AD†		C		GP		I		CS		M1		M2		OT		D	
DATA	Mean	SD	Mean	SD	Mean	SD	Mean	SD	Mean	SD	Mean	SD	Mean	SD	Mean	SD	Mean	SD
SIR-C 1994																		
- C-HH	−6.5a‡	0.9	−5.9a	0.7	−10.5b	1.7	−12.1c	2.1	−12.0c	1.0	−12.8c	2.0	−17.0e	2.0	−11.7c	1.8	−22.1f	2.0
- C-HV	−10.6b	1.0	−9.3b	1.1	−16.2d	1.9	−15.6d	1.9	−17.2e	1.8	−16.0d	2.0	−18.7e	1.9	−12.8c	2.0	−22.9f	1.6
- L-HH	−14.2d	1.7	−5.6a	1.5	−14.3d	1.8	−22.3g	2.3	−24.4g	1.9	−23.7g	2.2	−22.8g	2.1	−13.7d	2.6	−27.8h	1.9
- L-HV	−26.0h	1.7	−15.1d	1.7	−25.8h	1.9	−28.4h	2.1	−29.9h	2.0	−27.1h	2.4	−33.6h	2.1	−22.7g	2.7	−38.7i	1.9
ERS 1 1992																		
- C-VV	−6.8a	1.9	−6.2a	2.3	−7.7b	2.1	−6.3a	1.8	−15.1d	2.0	−6.1 a	2.3	−10.0b	2.5	−9.5ab	2.5	−17.5e	2.6
ERS 2 1998																		
- C-VV	−9.4ab	2.9	−6.7b	3.1	−11.3c	2.6	−7.7b	2.3	−18.5de	2.4	−8.1b	2.8	−16.0d	2.5	−16.5e	2.6	−18.5f	3.4
ERS 2 2001																		
- C-VV					−9.3b	2.2	−7.8b	2.0	−16.5e	2.1	−7.3b	2.3	−14.1d	3.0	−14.0d	2.5	−17.4e	2.6
–	−7.7b	2.9	−5.7a	2.1														
ERS 2 2002																		
- C-VV	−12.4c	3.1	−8.0b	3.4	−14.7d	2.6	−12.3c	2.8	−19.1f	2.5	−11.3c	2.8	−18.1e	3.0	−17.4e	2.9	−22.4g	3.4
ENVISAT 2004																		
- C-VV	−10.1c	3.1	−6.2a	3.2	−11.2c	3.0	−14.5d	3.6	−14.6d	3.0	−13.1d	3.2	−15.8d	2.7	−13.3d	3.2	−17.0e	3.4
- C-HH	−12.6d	3.4	−7.5b	3.1	−17.5e	3.1	−15.4e	3.6	−16.0e	3.0	−15.0e	3.6	−20.4f	3.1	−15.3e	3.6	−21.0f	3.4
ENVISAT 2006																		
- C-VV	−13.1d	3.4	−6.8b	3.1	−14.4d	3.2	−15.8e	3.6	−14.3d	3.0	−16.3e	3.0	−17.3e	2.1	−13.2d	3.5	−23.4g	3.4
- C-VH	−22.6g	3.6	−11.7c	3.1	−21.6g	3.2	−22.6g	3.4	−23.5g	3.5	−19.7f	3.6	−23.9g	3.5	−20.4f	3.5	−25.1h	3.0
RADARSAT 1 2005																		
- C-HH	−13.2d	3.2	−7.0a	2.4	−16.2d	2.3	−14.9d	3.1	−16.8e	3.0	−14.8d	3.3	−22.9g	3.0	−18.0e	3.1	−24.7h	3.2
ALOS PALSAR 2007																		
- L-HH	−11.8c	1.6	−7.1a	2.0	−17.4e	1.7	−20.4f	1.8	−22.2f	1.8	−15.1d	2.1	−22.8f	1.7	−13.3d	2.4	−27.2h	1.9
ALOS PALSAR 2008																		
- L-HH	−12.5bc	1.4	−7.7a	1.8	−18.0e	1.7	−22.3g	2.6	−23.1g	1.8	−16.4e	3.2	−23.7g	1.8	−12.4c	2.7	−28.1h	2.4

† AD: scald-scabby areas (deflation areas), C: cliff scarps (wind abrasion), GP: discontinuous thin aeolian mantles in gravel plains, I: interdunes, CS: closed scrubs, M1: mosaic grass-scrub steppe with deflation areas, M2: grass-scrub steppe without deflation areas, OT: old track sand dune, and D: active sand dune megapatches.

‡ Different letters indicate significant differences ($p < 0.05$) among classes.

the presence of aeolian features such as sand or dust sources (mostly bright), active dunes (dark with bright mottles), *reg* surfaces with desert pavement (intermediate gray tones), and sand mantles (alternating bright and dark narrow features). The brightness tones represent backscatter amplitude values. The mottled bright appearance of the active dunes results from quasi-specular returns from dune faces oriented normal to the radar illumination (incidence angle image of 23°).

The boundaries of the sand dune megapatches are sharp but not fully stable, as illustrated in Fig. 5a-d. However, there are some wind-related features that provide clues to the wind direction (Schaber, 1999). On Fig. 5c that represents a calm day, sandy areas appear dark due to their smooth texture, whereas interdune areas appear in gray tones. In contrast, Fig. 5d shows the influence of the wind blowing from west on sand mobilization (at wind speed of 8.1 m s^{-1}). Thus, large sand sheets are almost continuously swept over the land surface (Qong, 2000).

C-band Analysis: ERS-2, ENVISAT ASAR, and RADARSAT-1

A comparison between subsets of ERS-2, ENVISAT ASAR, and RADARSAT-1 images on Fig. 6a-d, shows the differences in dune visibility and brightness variations. The subtle visibility of inactive linear sand dunes (white arrows) is highly dependent on radar polarization, incidence angle, and viewing geometry. Linear sand dunes have dark to intermediate gray tones in C-VV images (Fig. 6a and Fig. 6c) probably because of the deposition of windblown material, which absorbs the radar signal and produces a lower digital number (Greeley et al., 1997). Comparatively, linear sand dunes appear slightly brighter in C-HH images. The look angle (23°) in both ERS-2 and ENVISAT ASAR images plays an important role in the delineation of active sand dunes by enhancing the surface roughness of the landforms. However, the ENVISAT ASAR images (Fig. 6b-c) seem to have a higher radiometric dynamics that allows discriminating the internal structure of the sand dune megapatches. In the case of thin discontinuous sand mantles that are locally stabilized by shrub, backscatter increases on RADARSAT-1 images (Fig. 6d) as a result of volume scattering from an argillic-calcic soil horizon and by volume scattering from the root mounds of shrubs (mostly *Chuquiraga avellanedae*) (Bouza et al., 2005). RADARSAT-1 (C-HH) shows a better backscatter contrast (image tone) for the various geologic, landform, and soil units.

L-band Analysis: SIR-C and ALOS PALSAR

Figure 7a-d shows the L-band from SIR-C and ALOS PALSAR, where stabilized sand deposits have clearly defined edges on radar images. Field observations indicate that they were deposited as sand sheets and large dunes. Thin white lines are bright reflections from steep sand ridge crests. The sand ridges, now smoothed and partially reworked, seem to have derived from a mixture of active and inactive barchanoid ridges and parabolic dunes. This suggests that there is a transition between both dune types as the

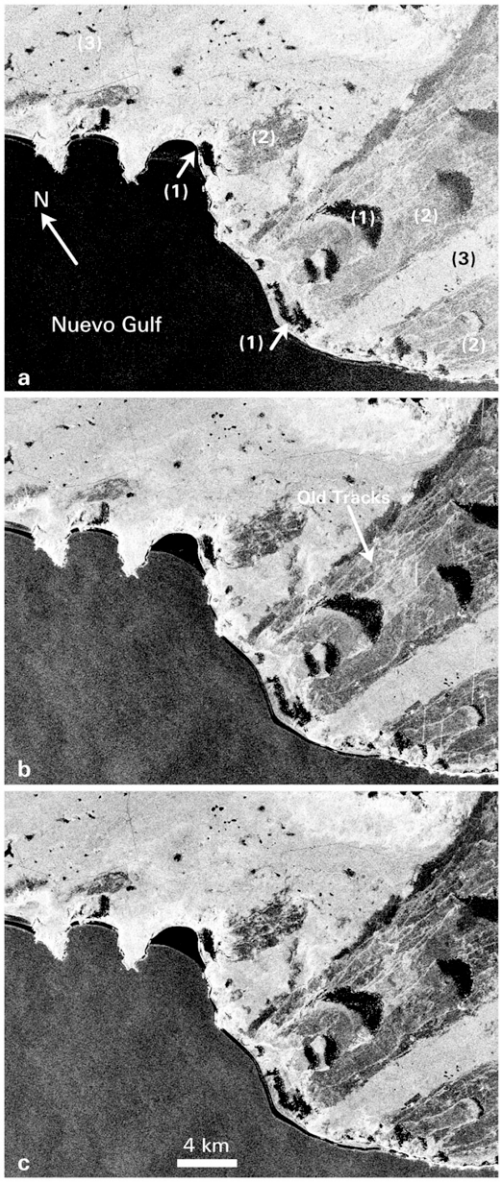

Figure 4a-c. Subsets of a SIR-C image acquired on 5 Oct. 1994 (4a: C-band HV, 4b: L-band HH, 4c: L-band HV). Radar illumination is from the left at an incidence angle of 55.8°. The following features can be observed: (1) smooth dry dark surfaces (active sand dunes), (2) intermediate shades of gray (stabilized dunefields) as a function of the interactions between soil moisture, surface roughness, and vegetation type (natural species), and (3) bright targets at or near saturation due to high volume and surface scattering (effects between plant, dune topography and incident microwaves). The white arrows point to thin white lines (bright reflections) from steep crests of the inactive sand ridges associated to the parabolic dunes (old tracks sand dune).

vegetation cover increases (Duran et al., 2008). That is a clear example of deactivation of migrating dunes under the influence of vegetation. These sand ridges, which represent old track dune systems, can be easily recognized from the L-band data, whereas only a few of the larger tracks are visible in the C-band data.

The contrast between dunes and interdune areas is greatest in the L-band from ALOS PALSAR (Fig. 7c and Fig. 7d). This is consistent with the pixel size that needs to be 10-m or more resolution to identify interdune details. Interdune areas are usually covered by a crust of fine particles and salts. However, the terrain surface is also modified by wind ripples (2–5 cm high) causing roughness that is well represented on the L-band. This band creates a much stronger contrast between the dunes and their surroundings.

On the L-HH band (Fig. 8a-b), stabilized sand units appear with intermediate and bright tones. The active sand dunes in megapatches are distinctively darker. The L-HH image response becomes progressively darker (like C-band) at incidence angles larger than 40° such as on SIR-C images (Schaber, 1999). Figure 8a shows the active sand dunes at the endpoint of the sand transport (Atlantic Ocean). Figure 8b highlights the negative impact of wind activity on rangeland production and farm infrastructure (private airport indicated by black arrows). The bright lines in Fig. 8b (black arrows) represent the inactive barchanoid ridges and parabolic dunes earlier described.

Old track dune systems are better-mapped using long wavelength (L-band) than short wavelength (C-band). The penetration depth of the C-band is 4.2 times less than that of the L-band, being <1 m even in very dry conditions (El-Baz and Robinson, 1997). Our results show better discrimination of the internal structure of the sand dune megapatches in the C-bands from ERS-2, ENVISAT ASAR, and RADARSAT-1 images, including the orientation of the dune slopes. A slight rise in backscatter at low incidence angle, approximately equal to the angle of repose of sand (Stephen and Long, 2004), reflects the presence of surficial sand slips. Images of the interdune areas show that the sub-10 m resolution of RADARSAT-1 is also sufficient to identify details of these flat areas.

Conclusions

In this study, we have explored the potential of different SAR sensors for the estimation of structural attributes of wind-driven land degradation processes in grazed dunefields. The visibility of aeolian features on radar images is mostly a function of wavelength, polarization, and incidence angle.

The active sand deposits in the Valdes Peninsula appear as dark areas at all wavelengths and polarizations. Stabilized sand deposits are clearly observed in radar images, with defined edges but also signals of ongoing wind erosion. Different classes showed differences in backscatter response mostly related to vegetation cover and wavelength-dependent surface roughness (wind activity that reworks unconsolidated surficial deposits). The effect of wind speed (≥ 4.0 m s^{-1}) on the target increases the backscatter value, being this wind speed usually considered as the threshold of wind erosion.

The backscatter is also controlled by changes in the local incidence angle and look direction (ascending vs. descending orbit). Smaller incidence angles (23–35°) tend to enhance the dune topography while a larger incidence angle (55.8°) makes the dune surface appear smooth. A descending orbit (west looking) shows the dunes and interdunes areas much better than an ascending orbit (east looking). An ascending orbit also decreases the visibility of some inactive and active linear dunes.

The longer wavelengths (L-band) distinguish mostly old track sand dunes and scald-scabby areas (deflation areas) bet-

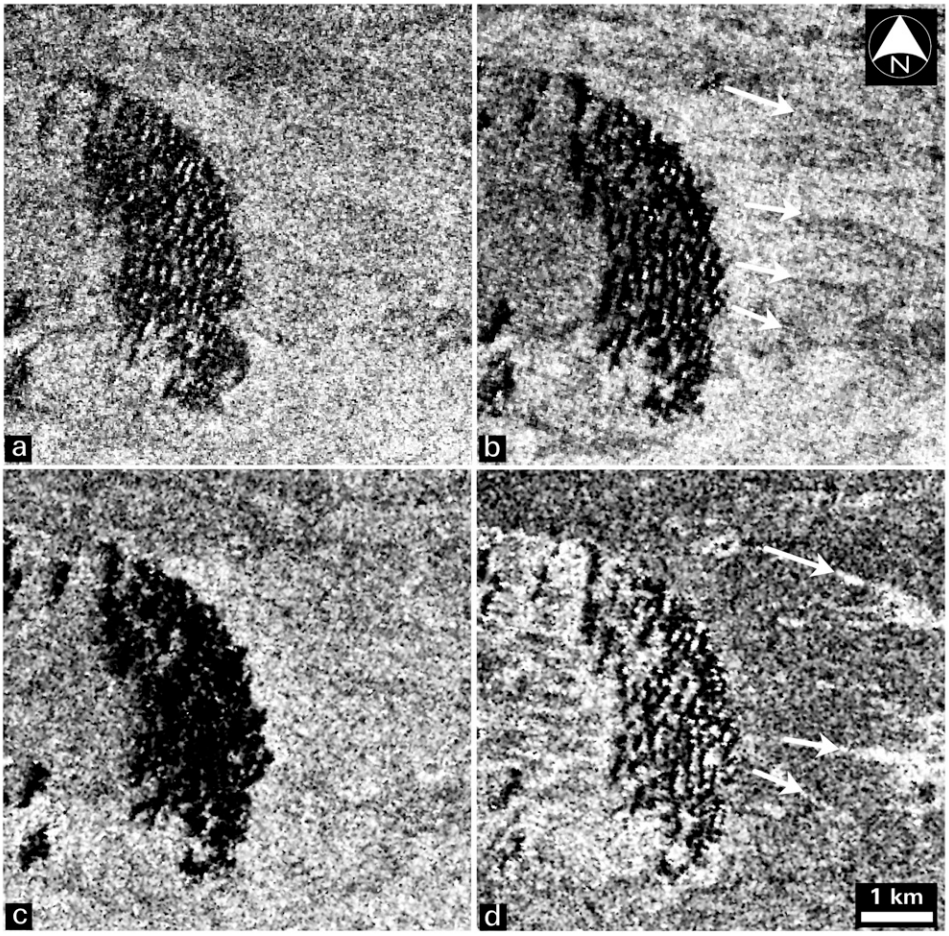

Figure 5a-d. Influence of the wind conditions on a sand dune megapatch and its surroundings, observed on a subset from ERS-1 and 2 images (C-VV). Wind causes local "noise" effect on the temporal backscatter signal. Radar illumination is from the right at an incidence angle of 23°. The mottled bright appearance of the active dunes results from quasi-specular returns from dune faces oriented normal to the radar illumination. The wind direction and the maximum wind speed at the time of taking the image are indicated in brackets for each figure (Source: Puerto Madryn, weather station). 5a. 9 July 1992 (SE, 3.1 m s^{-1}). 5b. 22 Feb.1998 (NE, 5.8 m s^{-1}). The dark lines on the brightness matrix, visible on the right of the figure, are linear dunes. 5c. 28 July of 2001 (SW, 2.1 m s^{-1}). The active dunes have dark tones; the linear dunes are not visible. 5d. 5 May 2002 (W, 8.1 m s^{-1}). The bright wind streaks denote zones of particle removal by the local turbulence of the wind.

ter than the shorter wavelengths (C-band) because of increased contrast. The old track sand dunes are a clear example of deactivation of migrating dunes under the influence of vegetation.

The old track sand dunes reveal aerodynamic roughness information that can be used in wider studies on aeolian processes, not only in the Valdes Peninsula. These features would allow mapping near-surface wind patterns. The lack of weather stations in the study area, especially wind data, could be partially overcome with these studies.

Although multipolarization and multiwavelength SAR data are recognized to be extremely useful for studying arid and semiarid environments, single and dual polarization SAR data, such as those provided by ERS-1 and 2, ENVISAT ASAR, and RADARSAT-1, can complement the data generated by satellites such as the present RADARSAT-2, ALOS PALSAR, TERRASAR-X, COSMO-SkyMed, and the forthcoming TERRASAR-L and SAOCOM.

Significant challenges still exist for radar imagery to achieve its full potential for wind-driven land degradation processes. From the remote sensing perspective, several issues need to be addressed. The full range of factors which result in spatial and temporally varying signatures on SAR imagery still have to be quantified, with the influence of wind conditions, and plant cover being the principal uncertainties. Obviously, the combination of optical data with radar data (data fusion) is fundamental for a synergic approach. Data fusion represents a strategic way to increase the potentialities of remote sensing in real-world applications thanks to the promise of improvement in accuracy and reliability of analysis results.

The approach implemented in this study can be applied elsewhere to obtain a better understanding of the scattering mechanisms, sensor and target parameters, and their influence on the SAR backscatter from aeolian targets, and improve our comprehension of wind-driven land degradation processes in mid-latitude regions.

Acknowledgments

This work was financial supported by the Consejo Nacional de Investigaciones Científicas y Técnicas (CONICET), National Research Initiatives, Grant PIP 6413. Argentina's National Commission on Space Activities (CONAE) supplied the ERS-1,

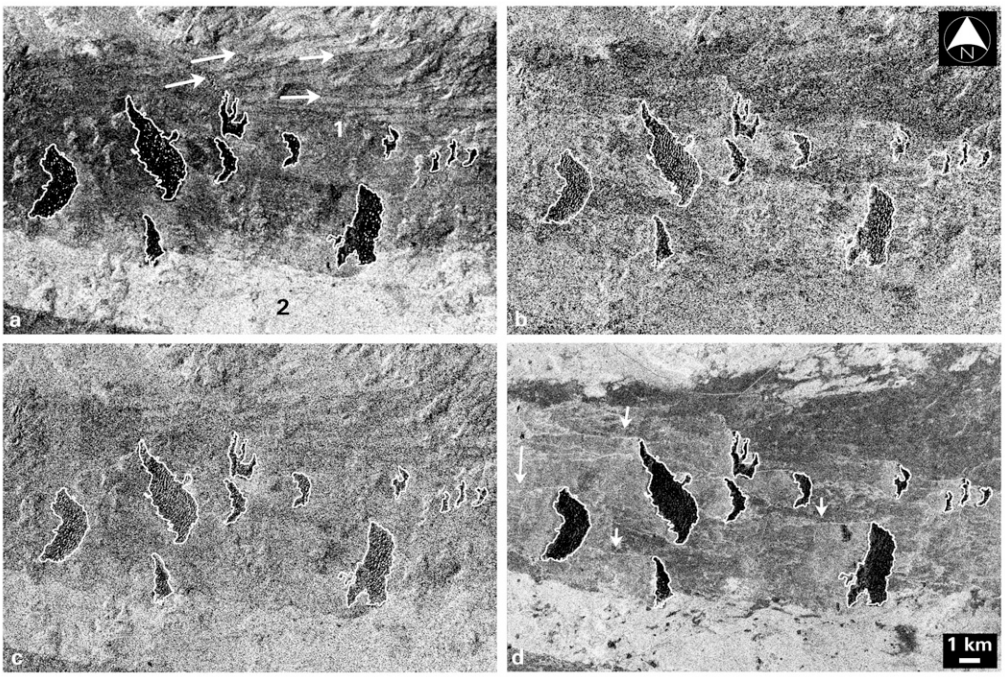

Figure 6a-d. Like- and cross-polarized radar subset image at C-band in the center of the WE dunefields. 6a. ERS-2 C-band VV. White arrows indicate inactive linear sand dunes. 1. Dunefield WE. 2. Discontinuous thin aeolian mantle in gravel plain. 6b-c. ENVISAT ASAR C-bands VV (6b) and VH (6c). Note the internal structure of the sand dune megapatches. 6d. RADARSAT-1 C-band HH. White arrows indicate old track sand dunes.

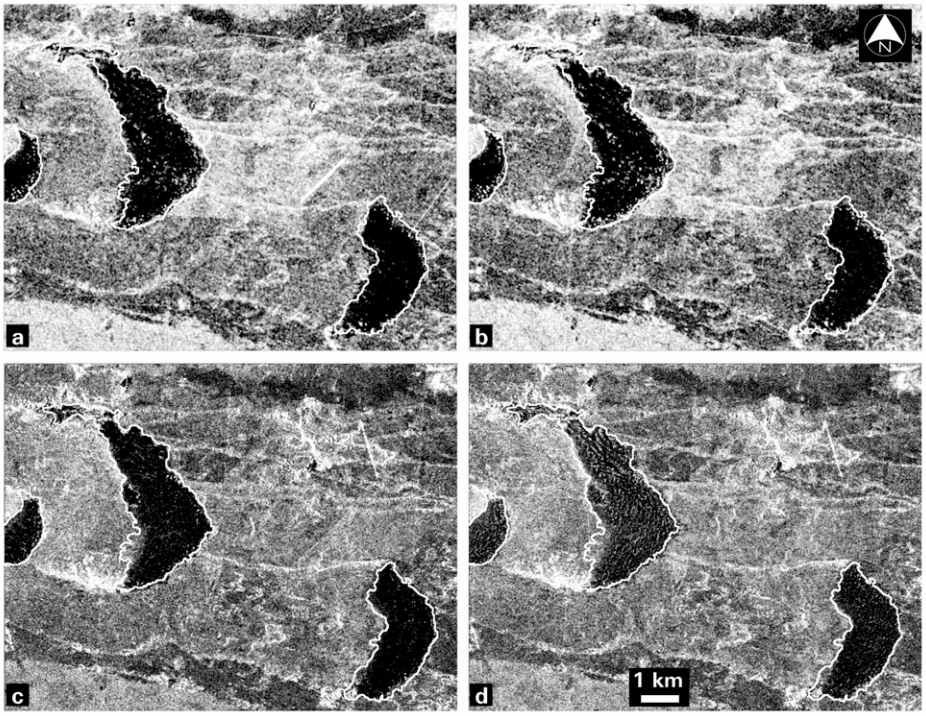

Figure 7a-d. Comparison of information content in SAR data with like-polarization (HH) and cross-polarization (HV) of the L-band. Radar illumination is from the left at incidence angles of 55.8° (7a-b) and 34.3° (7c-d). 7a-b. Subset of an image acquired by the SIR-C mission on 5 Oct. 1994. 7c-d. Subsets form ALOS PALSAR images (L-HH) acquired on 14 Feb. 2007 and 17 Feb. 2008.

ERS-2, RADARSAT-1, and ALOS PALSAR images, within the framework of the Airborne Synthetic Aperture Radar (SARAT) project. The Argentina-Germany Technical Cooperation provided the SIR-C images within a GTZ-Universität München-CENPAT (CONICET)-UNPSJB project. Dr. D.A. Gagliardini (CENPAT, CONICET) provided the ENVISAT ASAR images

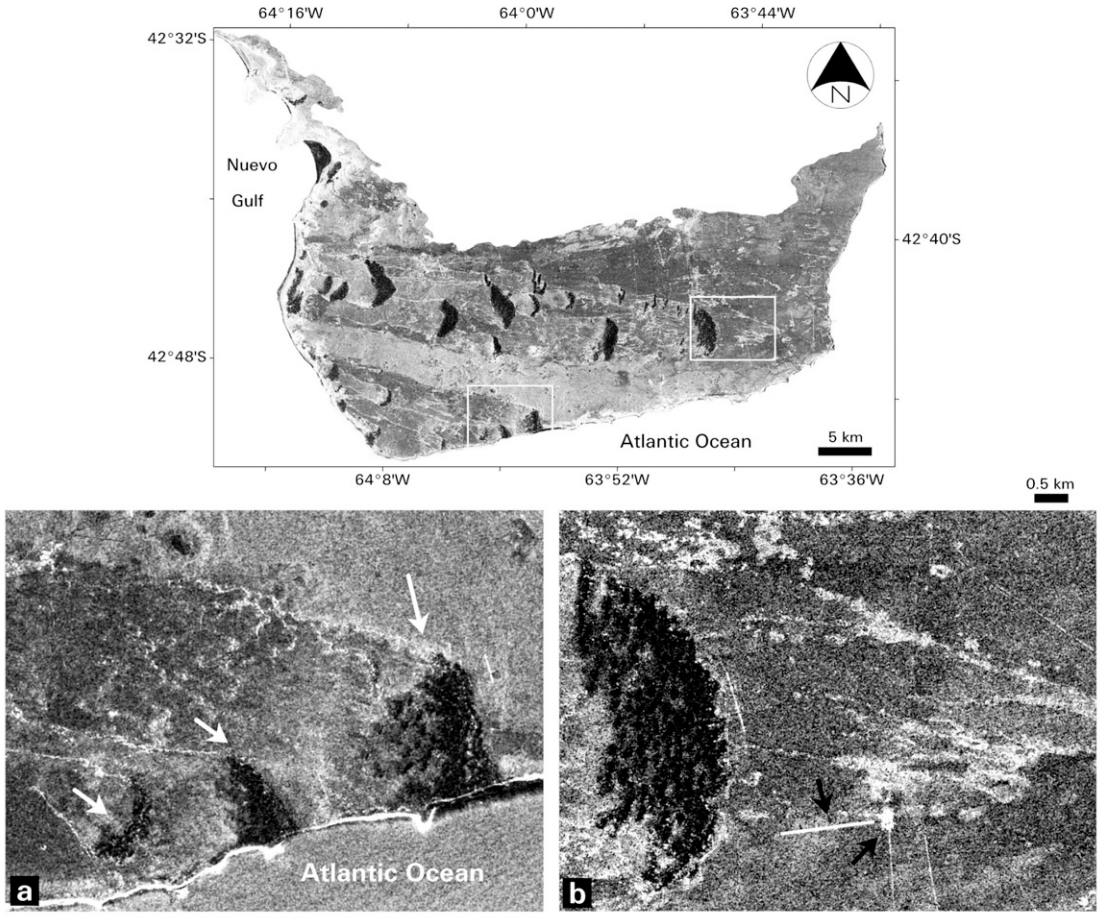

Figure 8a-b. Like-polarized subset image of from ALOS PALSAR (L-band HH) in the WE and SW dunefields. 8a. White arrows indicate the active sand dune megapatches at the endpoint of the sand transport (Atlantic Ocean). 8b. Impact of wind activity on rangeland production and farm infrastructure (private airport indicated by black arrows).

within a project from European Space Agency (ESA): "Integrated Analysis of Ocean-Coastal-Land Ecosystems by ENVISAT-1 Data for the Characterization of Argentine Coastal Regions".

References

Barros, V., and M.M. Rivero. 1982. Mapas de probabilidad de precipitación en la Provincia del Chubut. Contribución no. 54. CENPAT (CONICET), Puerto Madryn, Chubut, Argentina (In Portuguese.)

Bertiller, M.B., A.M. Beeskow, and M.P. Irisarri. 1981. Caracteres fisonómicos y florísticos de vegetación del Chubut: 2. La Península Valdés y el Istmo Ameghino. Contribución no. 41. CENPAT (CONICET), Puerto Madryn, Chubut, Argentina. (In Portuguese).

Blanco, P.D., G.I. Metternicht, and H.F. del Valle. 2009. Improving the discrimination of vegetation and landform patterns in sandy rangelands: A synergistic approach. Int. J. Remote Sens. 30:2579–2605.

Blanco, P.D., C.M. Rostagno, H.F. del Valle, A.M. Beeskow, and T. Wiegand. 2008. Grazing impacts in vegetated dunefields: Predictions from spatial pattern analysis. Rangeland Ecol. Manage. 61:194–203.

Blom, R., and C. Elachi. 1981. Spaceborne and airborne imaging radar observation of sand dunes. J. Geophys. Res. 86:3061–3073.

Blumberg, D.G. 1998. Remote sensing of desert dune forms by polarimetric Synthetic Aperture Radar (SAR). Remote Sens. Environ. 65:204–216.

Blumberg, D.G., T. Neta, N. Margalit, M. Lazar, and V. Freilikher. 2004. Mapping exposed and burial drainage systems using remote sensing in the Negev desert, Israel. Geomorphology 61:239–250.

Bouza, P., M. Simón Torres, J. Aguilar Ruiz, C.M. Rostagno, and H.F. del Valle. 2005. Genesis of some selected soils in the Valdes Peninsula, NE Patagonia, Argentina. p. 1–12. *In* A. Faz Cano et al. (ed.) Advances in geoecology 36: Genesis, classification and cartography of soils. Catena Verlag GMBH, Reiskirchen, Germany.

Bouza, P.J., M. Simón Torres, and C.M. Rostagno, J. Aguilar Ruiz, and H.F. del Valle. 2002. Propiedades físicas, químicas y mineralógicas de aridisoles en península Valdés. XVIII Congreso Argentino de la Ciencia del Suelo, Puerto Madryn (Chubut). 16–19 Apr. 2002. CD-ROM. Asociación Argentina de Ciencia del Suelo, Puerto Madryn (Chubut), Argentina.

Carter, D.J., and H.J. Houghton. 1981, Remote sensing of wind erosion in croplands. p. 275–282. *In* P. Laut (ed.) Proc. of Landsat- 81 Conf., Canberra, Australia. Organizing Committee, Canberra, A.C.T.

Chadwick, O.A., L.A. Derry, P.M. Vitousek, B.J. Huebert, and L.O. Hedin. 1999. Changing sources of nutrients during four million years of ecosystem development. Nature (London) 397:491–497.

Chen, Z., C.D. Elvidge, and D.P. Groenveld. 1998. Monitoring of seasonal dynamics of arid land vegetation using AVIRIS data. Remote Sens. Environ. 65:255–266.

Collado, A.D., E. Chuvieco, and A. Camarasa. 2002. Satellite remote sensing analysis to monitor desertification processes in the crop-rangeland boundary of Argentina. J. Arid Environ. 52:121–133.

CSA. 2000. 2000. RADARSAT Data Products Specifications. RADARSAT International. RSI-GS-026. Revision 3(0):125.

Defossé, G.E., M.B. Bertiller, and C.M. Rostagno. 1992. Rangeland management in Patagonian drylands. p. 12–21. *In* G.K. Perrier and C.W. Gay (ed.) Proc. of the 1992 Int. Rangeland Development Symp., Spokane, WA. Soc. for Range Management, Spokane, WA.

del Valle, H.F., and P.D. Blanco. 2006. Indicadores espectrales del rango de las microondas para la evaluación y monitoreo de la erosión eólica. p. 65–84. *In* E.M. Abraham and G. Beekman (ed.) Indicadores de la desertificación

para América del Sur, Recopilación y armonización de indicadores y puntos de referencia de la desertificación a ser utilizados en el programa: Combate a la desertificación y mitigación de los efectos de la sequía en América del Sur. IICA-BID ATN JF 7905-RG. Inst. Interamericano de Coop. para la Agric., Mendoza, Argentina. (In Portuguese.)

del Valle, H.F., P.D. Blanco, W. Sione, C.M. Rostagno, and N.O. Elissalde. 2009. Assessment of salt-affected soils using multisensor radar data: A case study from northeastern Patagonia (Argentina). p. 155–173. *In* G.I. Metternicht and J.A. Zinck (ed.) Remote sensing of soil salinization: Impact on land management. CRC Press/Taylor & Francis Group, Boca Raton, FL.

del Valle, H.F., C.M. Rostagno, and P.J. Bouza. 2000. Los médanos del sur de Península Valdés: Su dinámica y los cambios asociados en los suelos y en la vegetación (Comisión V, versión CD ROM, 6 pages in pdf format). XVII Congreso Argentino de la Ciencia del Suelo.11–14 Apr. 2000. Asoc. Argentina de la Ciencia del Suelo, Mar del Plata (Bs. As.), Argentina.

del Valle, H.F., C.M. Rostagno, F.R. Coronato, P.J. Bouza, and P.D. Blanco. 2008. Sand dune activity in north-eastern Patagonia. J. Arid Environ. 72:411–422.

Desnos, Y.L., C. Buck, J. Guijarro, J.L. Suchail, R. Torres, and E. Attema. 2000. ASAR– Envisat's advanced synthetic aperture radar: Building on ERS achievements towards future earth watch missions. ESA Bull. 102:91–100.

Dobson, M.C., L.E. Pierce, and F.T. Ulaby. 1997. The role of frequency and polarization in terrain classification using SAR data. p. 1621–1623. *In* T.L. Stein (ed.) Remote sensing—A scientific vision for sustainable development. Proc., Int. Geoscience Remote Sensing Symp., Proc., Vol. 4, New York. May 1997. Int. Geoscience and Remote Sensing Soc., New York.

Dobson, M.C., L.E. Pierce, and F.T. Ulaby. 1995. Knowledge-based land-cover classification using ERS-1/JERS-1 SAR composites. IEEE Trans. Geosci. Remote Sens. 34:83–99.

Duran, O., M.V.N. Silva, L.J.C. Bezerra, H.J. Hermann, and L.P. Maia. 2008. Measurements and numerical simulations of the degree of activity and vegetation cover on parabolic dunes in north-eastern Brazil. Geomorphology 102:460–471.

El-Baz, F., and C.A. Robinson. 1997. Paleo-channels revealed by SIR-C data in the Western Desert of Egypt: Implications to sand dune accumulations. p. 469–476. *In* 12th Int. Conf. on Applied Geologic Remote Sensing, Vol. 1, Denver, CO. 17–19 Nov. 1997. Environ. Res. Inst. of Michigan, Ann Arbor.

ERDAS Inc. 2008. Erdas field guide. ERDAS IMAGINE, version 9.2. Available at http://www.erdas.com/. (verified 22 Oct. 2009). Leica Geosystems Geospatial Imaging, LLC, Norcross, GA.

Freeman, A. 1995. SIR-C/X data quality and calibration results. IEEE Trans. Geosci. Remote Sens. 33:848–857.

Fung, A.K. 1994. Microwave scattering and emission models and their applications. Artech House, Boston, MA.

Gagliardini, D.A., A. Súnico, P.J. Bouza, and H.F. del Valle. 1994. Geomorphology of Península Valdés based on ERS-1 image interpretation. p. 228–234. *In* Vol. 30, Part 7a, Proc., Int. Symp. on Resource and Environmental Monitoring, Río de Janeiro, Brazil. 26–30 Sept. 1994. Int. Soc. For Photogrammetry and Remote Sensing, Río de Janeiro, Brazil.

Gibbens, R.P., J.M. Tromble, J.T. Hennessy, and M. Cardenas. 1983. Soil movement in mesquite dunelands and former grasslands of southern New Mexico from 1933 to 1980. J. Range Manage. 36:145–148.

Greeley, R., and D.G. Blumberg. 1995. Preliminary analysis of Shuttle Radar Laboratory (SRL-1) data to study aeolian features and processes. IEEE Trans. Geosci. Remote Sens. 3:927–933.

Greeley, R., D.G. Blumberg, J.F. Mc, A. Hone, J.D. Dobrovolskis, N. Iversen, N. Lancaster, K.R. Rasmussen, S.D. Wall, and B.R. White. 1997. Applications of space borne radar laboratory data to the study of aeolian processes. J. Geophys. Res. 102:10971–10983.

Haller, M.J., A.J. Monti, and C.M. Meister. 2000. Hoja Geológica 4363-I: Península Valdés, Provincia del Chubut. Programa Nacional de Cartas Geológicas de la República Argentina, 1:250000. Boletín no. 266. Servicio Geológico Minero Argentino, Buenos Aires, Argentina.

Iriondo, M.H., and N.O. García. 1993. Climatic variations in the Argentine plains during the last 18 000 years. Palaeogeogr. Palaeoclimatol. Palaeoecol. 101:209–220.

JAXA. 2008. ALOS Data users handbook. Revision C. March 2008. Earth Observation Res. and Application Ctr., Japan Aerospace Exploration Agency. Alaska Satellite Facility, User Services Office, Alaska.

Kasischke, E.S., J.M. Melack, and M.C. Dobson. 1997. The use of imaging radars for ecological applications: A review. Remote Sens. Environ. 59:141–156.

Lancaster, N., L. Gaddis, and R. Greeley. 1992. New airborne imaging radar observations of sand dunes: Kelso dunes, California. Remote Sens. Environ. 39:233–238.

Lal, R. 2001. Soil degradation by erosion. Land Degrad. Rehabil. 12:519–539.

Laur, H., P. Bally, P. Meadows, J. Sanchez, B. Schaettler, E. Lopinto, and D. Esteban. 2004. Derivation of the backscattering coefficient σ^o in ESA ERS PRI products. Doc. no: ES-TN-RS-PM-HL09 05, Issue 2. Rev. 5f:53. European Space Agency, Frascati, Italy.

León, R.J.C., D. Bran, M. Collantes, J.M. Paruelo, and A. Soriano. 1998. Grandes unidades de vegetación de la Patagonia extrandina. Ecol. Aust. 8:275–308.

Levin, N., E. Ben-Dor, G.J. Kidron, and Y. Yaakov. 2008. Estimation of surface roughness (Zo) over a stabilizing coastal dune field based on vegetation and topography. Earth Surf. Processes Landforms 33:1520–1541.

Liu, J.G., R. Capes, M. Haynes, and J. Mc. Moore. 1997. ERS SAR multi-temporal coherence image as a tool for sand desert study (dune movement, sand encroachment and erosion). p. 478–485. *In* Proc. 12th Int. Conf. and Workshop on Applied Geological Remote Sensing, Vol. 1, Denver, CO. 17 June–19 Nov. 1997. ERIM, Ann. Arbor, MI.

Ogawa, K., T. Schmugge, F. Jacob, and A. French. 2002. Estimation of land surface window emissivity from multi-spectral thermal infrared remote sensing: A case study in part of the Sahara Desert. Agronomie 22:595–696.

Okin, G.S., and D.A. Gillette. 2001. Distribution of vegetation in wind-dominated landscapes: Implications for wind erosion modeling and landscape processes. J. Geophys. Res. 106:9673–9683.

Okin, G.S., B. Murray, and W.H. Schlesinger. 2001. Degradation of sandy arid shrubland environments: Observations, process modeling, and management implications. J. Arid Environ. 47:123–144.

Paisley, E.C.I., N. Lancaster, L.R. Gaddis, and R. Greeley. 1991. Discrimination of active and inactive sand from remote sensing: Kelso Dunes, Mojave Desert, California. Remote Sens. Environ. 37:153–166.

Paruelo, J.M., A.B. Beltrán, E.G. Jobbagy, O.E. Sala, and R.A. Golluscio. 1998. The climate of Patagonia: General patterns controls on biotic processes. Ecol. Aust. 8:85–101.

Prigent, C., I. Tegen, F. Aires, B. Marticorena, and M. Zribi. 2005. Estimation of the aerodynamic roughness length in arid and semi-arid regions over the globe with the ERS scatterometer. J. Geophys. Res. 110:1–12.

Prospero, J.M., P. Ginoux, O. Torres, S.E. Nicholson, and T.E. Gill. 2002. Environmental characterization of global sources of atmospheric soil dust identified with the NIMBUS 7 Total Ozone Mapping Spectrometer (TOMS) absorbing aerosol product. Rev. Geophys. 40:1–31.

Qong, M. 2000. Sand dune attributes estimated from SAR images. Remote Sens. Environ. 74:217–228.

Ramsey, M.S., P.R. Christensen, N. Lancaster, and D.A. Howard. 1999. Identification of sand sources and transport pathways at the Kelso Dunes, California using thermal infrared remote sensing. Geol. Soc. Am. Bull. 111:646–662.

Ridley, J., F. Strawbridge, R. Card, and H. Phillips. 1996. Radar backscatter characteristics of a desert surface. Remote Sens. Environ. 57:63–78.

Rostagno, C.M. 1981. Reconocimiento de suelos de Península Valdés. Contribution no. 44. CENPAT (CONICET), Puerto Madryn, Chubut, Argentina. (In Portuguese.)

Schaber, G.G. 1999. SAR studies in the Yuma Desert, Arizona: San penetration, Geology, and the detection of military ordnance debris. Remote Sens. Environ. 67:320–347.

Sheng, Y., and Z.G. Xia. 1996. A comprehensive evaluation of filters for radar speckle suppression. p. 1559–1561. *In* Remote sensing for a sustainable future. Vol. 3. Geosciences and Remote Sensing Symp. Proc.GRSS, Lincoln, NE.

Stephen, H., and D.G. Long. 2004. Analysis of scatterometer observations of Saharan Ergs using a simple rough facet model. IEEE Trans. Geosci. Remote Sens. 1534–1537.

Súnico, A. 1996. Geología del Cuaternario y Ciencia del Suelo: Relaciones geomórficas- estratigráficas con suelos y paleosuelos (Quaternary Geology and Soil Science: Geomorphic-stratigraphic relations with soils and paleosoils). Ph.D. thesis. Univ. Nacional de Buenos Aires (UBA), Argentina.

Trombotto, D. 1998. Paleo-permafrost in Patagonia. Bamberger Geogr. Schriften 15:133–148.

USDA. 2003. Keys to soil taxonomy. 9th ed. USDA, Natural Resources Conserv. Serv. (NRCS), Washington, DC.

van Zyl, J.J., and F.T. Ulaby. 1990. Scattering matrix representations for simple targets. p. 17–52. *In* Radar polarimetry for geoscience applications. Artech House, Norwood, MA.

Zobeck, T.M., N.C. Parker, S. Haskell, and K. Guoding. 2000. Scaling up from field to region for wind erosion prediction using a field-scale wind erosion model and GIS. Agric. Ecosyst. Environ. 82:247–259.